Phase selection in aluminum rare-earth metallic alloys by molecular dynamics simulations using machine learning interatomic potentials

Ling Tang [1], Mathew J. Kramer,[2] Kai-Ming Ho,[2,3] and Cai-Zhang Wang [2,3,*]

[1]*Department of Applied Physics, College of Science, Zhejiang University of Technology, Hangzhou 310023, China*

[2]*Ames Laboratory-USDOE, Iowa State University, Ames, Iowa 50011, USA*

[3]*Department of Physics and Astronomy, Iowa State University, Ames, Iowa 50011, USA*

(Received 5 September 2022; revised 11 December 2022; accepted 9 January 2023; published 17 February 2023)

Aluminum rare-earth (Al-RE) metallic alloys and glasses with Al-rich compositions have attracted much attention owing to their high strength-to-weight ratio and superior thermal stability. However, differences in phase selection and formation upon using light- or heavy-RE elements are still not well understood. Using $Al_{90}Ce_{10}$ and $Al_{90}Tb_{10}$ as prototype Al-rich light-RE and heavy-RE alloys, we study the similarity and difference of phase selection and glass-formation ability (GFA) in the two metallic glasses by molecular dynamics (MD) simulations using accurate machine learning (ML) interatomic potentials and cluster alignment analysis. We show that the glass-forming structural short-range order (SRO) motifs are much stronger in $Al_{90}Tb_{10}$ glass than in $Al_{90}Ce_{10}$ glass (77% vs 47%). On the other hand, there is a noticeable fraction of $Al_{11}RE_3$ and hexagonal Al_3RE crystalline SRO motifs in $Al_{90}Ce_{10}$ glass that are almost absent in $Al_{90}Tb_{10}$. The origin of the SRO difference is investigated by comparing the structure-energy landscapes in these two systems, where unique competing metastable structures are obtained from an adaptive genetic algorithm search. MD simulations using the ML potentials and a solid/liquid interface model are also performed to show that the crystal growth speed in the Al-Ce is about 2-3 times faster than that in the Al-Tb system at similar undercooling conditions. The diffusion constant in the undercooled liquids and the latent heat of several competing crystalline phases and their liquids are also calculated to elucidate the different crystallization behaviors in the two systems. Moreover, chemical order preference in the two systems is also analyzed. Our results suggest that the different phase selection and GFA in the two systems can be attributed to the relative energetic stabilities of various competing metastable phases which lead to different structural and chemical SROs and different crystallization driving forces which influence the phase selection kinetics of the two systems.

DOI: 10.1103/PhysRevMaterials.7.025601

I. INTRODUCTION

Light-weight high-temperature alloys are important to the transportation industry. In designing energy-efficient vehicles and airplanes, the weight, cost, and operating temperature of the alloys are major factors of consideration. Aluminum rare-earth (Al-RE) metallic alloys and glasses with Al-rich compositions have attracted much attention owing to their high strength-to-weight ratio. With more than 85 at. % Al and under rapid cooling, Al-RE alloys can form either metallic glass or metastable crystalline compounds in the process of solidification, depending on the details of cooling rates and protocols [1].

The formation of metallic glasses around $Al_{90}RE_{10}$ compositions has been extensively studied in the past several decades [2–12]. It has been shown that the glass-formation ability (GFA) in these systems varies considerably with the RE elements. The best binary Al-RE glass formers are Al-Sm and Al-Tb, while Al-Ce alloy has a much weaker GFA. Recently, it has been shown that alloying aluminum with cerium can produce crystalline alloys with dramatically improved high-temperature performance, which are easily cast or readily "printed" using additive manufacturing compatible to traditional aluminum alloy additions [13–15]. Al-Ce based alloys have the potential to replace heavier steel and cast iron for use in elevated-temperature applications beyond current Al alloys. Understanding the fundamental interactions and mechanism governing the phase selection and stability in Al-RE based systems is therefore highly desirable for guiding the design, discovery, and synthesis of alternative Al-RE binary and Al-RE-X (X = Mg, Zr, $\cdots$) ternary intermetallic compounds for energy-efficient applications. In particular, La and Ce are "in excess supply" relative to the other REs [16,17]. More high-value uses for these abundant REs in alloy design will provide a more robust market for the RE industry.

Many questions about the role of different RE elements played in the phase selection and thermodynamic stability of Al-RE based alloys remain open. These questions include the following: what is fundamentally different between light RE (LRE) and heavy RE (HRE), and what roles do size and valence play in the phase selection and stability? More specifically, it is vital to understand the following questions: (a) How are the short-range order (SRO) and medium-range order (MRO) in the liquids and during the rapid solidification

*Corresponding author: wangcz@ameslab.gov

affected by different RE elements in Al-RE based alloys? (b) What are the local structure motifs in competing stable and metastable crystalline phases of Al-RE based alloys with different RE elements, and can the differences in the ground state structures tell us about GFA? (c) How do different RE elements in Al-RE based alloys influence the nucleation and growth kinetics of various competing crystalline phases?

While many experimental efforts have been devoted to investigating the local structure order in metallic glasses [1,18,19], elucidating the detailed atomic structure in terms of SRO and MRO is still very challenging for experimental studies. On the other hand, in the last 10 years, we have demonstrated that integrating molecular dynamics (MD) simulations with the local structure order analysis using the cluster alignment method [20] can provide a very powerful approach to quantifying the SRO and MRO in metallic liquids and glasses at the atomic scale [21–23]. More importantly, MD simulations can also provide critical insight into the mechanisms controlling kinetics nucleation and growth [24]. However, the bottleneck in MD simulation studies is the availability of the reliable interatomic potentials for the systems of interest.

Recently, we have shown that accurate and transferable interatomic potentials for Al-RE systems can be developed through a deep machine learning (ML) strategy using an artificial neural network (ANN) [25]. Such ANN-ML interatomic potentials have been successfully generated for Al-Tb and Al-Ce systems [26–28]. The ANN-ML potential for an Al-Tb system has also been used to perform MD simulations to investigate SRO and MRO in $Al_{90}Tb_{10}$ undercooled liquid and glass [26,27]. We show that the SRO in $Al_{90}Tb_{10}$ undercooled liquid and glass is strongly correlated with the building blocks of several unique low-energy metastable crystalline structures in the vicinity of the $Al_{90}Tb_{10}$ composition [27]. However, none of these SRO motifs matches well with the structures of the stable $Al_{11}RE_3$ or Al_3RE phases which are known to be common stable crystalline phases of Al-LRE and Al-RE alloys, respectively.

In order to understand the difference in GFA and phase selection in Al-rich alloys with LRE or HRE, in this paper we use $Al_{90}Ce_{10}$ and $Al_{90}Tb_{10}$ as prototypes for Al-LRE and Al-HRE metallic alloys and performed detailed analysis for the SRO and MRO differences in $Al_{90}Ce_{10}$ and $Al_{90}Tb_{10}$ glasses. Both glass samples are generated by MD simulations using the reliable ANN-ML interatomic potentials, and cluster alignment analysis is performed to quantify the SRO and MRO in the two systems. We also performed crystal structure predictions based on the adaptive genetic algorithm (AGA) and ANN-ML interatomic potentials to search for alternative energetically favorable metastable structures around the composition of $Al_{90}RE_{10}$. The results from our AGA search provide comprehensive energy landscapes which are very useful for understanding the thermodynamic driving forces for the phase selections in the two systems. Finally, we performed MD simulations (using the ANN-ML potentials) to study the crystallization process in the two systems to elucidate possible kinetic factors influencing the phase selection.

The results from our simulations and analysis show that although a large fraction of glass-forming motifs is also observed in $Al_{90}Ce_{10}$ glass, the percentage of such motifs is substantially smaller than that in $Al_{90}Tb_{10}$ glass. On the other hand, there is a noticeable fraction ($\sim$24%) of $Al_{11}RE_3$ crystalline SRO motifs in $Al_{90}Ce_{10}$ glass which are almost absent in $Al_{90}Tb_{10}$ glass, which is not surprising since the $Al_{11}RE_3$ is not a stable phase in HRE binary systems [29]. Moreover, about 10% of the Ce-centered SRO clusters in $Al_{90}Ce_{10}$ glass belong to the hexagonal Al_3Ce crystalline motif, while such clusters in $Al_{90}Tb_{10}$ glass are only about 2%. Crystal structure prediction using AGA also confirms that crystal structures with building blocks similar to the motifs of $Al_{11}RE_3$ crystal structure are energetically more favorable in the Al-Ce system than in the Al-Tb system. The difference in the relative energy landscapes in the two systems would lead to different phase selection behaviors during the solidification process. We also found that the Tb-Al bond lengths of the glass-forming SRO motifs in the glass are very different ($\sim$7.0% in average) from that of the nearby stable Al_3Tb phase, which would make the crystallization in Al-Tb system more difficult. Our MD simulation of crystallization from the solid-liquid interfaces also confirms that crystal growth proceeds faster in the Al-Ce system than in the Al-Tb system. Our simulation results thus provide useful insights for understanding the different GFA and phase selection in Al-LRE and Al-HRE systems.

The paper is arranged as follows. In Sec. II, we describe the computational methods used in our MD simulations and the SRO and MRO structure analyses. Methods for searching the lower-energy crystalline structures including AGA and *ab initio* calculations are also briefly described in Sec. II. The results obtained from our computational studies analyses, for given chemical compositions, including the SRO and MRO in the two glasses as well as structure-energy landscapes and comparison of crystal growth kinetics in the two systems, are presented and discussed in Sec. III. Finally, a summary is given in Sec. IV.

II. COMPUTATIONAL METHODS

MD simulations. MD simulations to generate $Al_{90}Ce_{10}$/$Al_{90}Tb_{10}$ glass samples and to study crystal growth at solid/liquid interfaces are performed using ANN-ML interatomic potentials and the LAMMPS package [30]. Our ANN-ML interatomic potentials for Al-Ce and Al-Tb systems developed [26,28] previously are further refined by including more training data from metastable crystalline structures through the AGA scheme described below so that the ANN-ML interatomic potentials describe accurately not only liquid and glass structures but also crystalline structures with various bonding topologies. The updated accurate and transferable ANN-ML potentials for Al-Ce and Al-Tb alloys are provided in the present Supplemental Material [31]. Atomistic structures of $Al_{90}Ce_{10}$/$Al_{90}Tb_{10}$ glass samples are generated by cooling from liquid states using 5000 atoms (4500 Al and 500 Ce or Tb) and with periodic boundary conditions. An isothermal-isobaric (*NPT*) ensemble at zero pressure and a Nosé-Hoover thermostat [32,33] are used in the simulations. The MD time step is taken as 2.5 fs. The liquid $Al_{90}Tb_{10}$ and $Al_{90}Ce_{10}$ samples are equilibrated at 2000 K for 500 ps, respectively, and then are continuously cooled down to

300 K at cooling rates of 10^{10} K/s. The sample configurations averaged over 500 ps at 300 K are used to analyze the structure order in glassy $Al_{90}Tb_{10}$ and $Al_{90}Ce_{10}$ by the template cluster alignment method. MD simulations of crystallization at solid/liquid interfaces are performed using the same LAMMPS package, the same ANN-ML potentials, and the same time step of 2.5 fs. More details of these simulations are given in Sec. III C.

SRO and MRO analysis. In order to investigate the local SRO and MRO in the glass samples generated by the MD simulations, the template cluster alignment method previously developed [20] is employed. Quasispherical clusters with a size of 70 atoms covering at least three atomic shells around each RE atom in the $Al_{90}RE_{10}$ samples from the MD simulations are extracted. We refer to these atomic clusters as sample clusters. A similar alignment scheme is also applied to Al-centered clusters as discussed in the Supplemental Material [31]. The first atomic shell of these sample clusters is then aligned one-by-one against several given templates (which are clusters containing only the first shell atoms around the center atom) to see how the SRO of the clusters extracted from the MD samples are similar to each of the given templates, respectively. The similarity is measured by an alignment score s which is defined as

$$s = \min_{0.8\leqslant\alpha\leqslant 1.2}\left\{\left[\frac{1}{N}\sum_{i=1}^{N}\frac{(\vec{r}_{ic}-\alpha\vec{r}_{it})^2}{(\alpha\vec{r}_{it})^2}\right]^{1/2}\right\}, \qquad (1)$$

where N is the number of the first shell atoms in the template. $\vec{r}_{ic}$ and $\vec{r}_{it}$ are the atomic positions in the sample cluster and template, respectively. α is chosen between 0.8 and 1.2 to vary the size of the template for an optimal alignment. From the alignment score defined in Eq. (1), we can see that the smaller the value of s is, the more similar is the sample cluster to the template. The alignment is performed by simulated annealing to minimize the alignment score s, using molecular dynamics simulations with a strong attractive potential between a pair of atoms in the sample cluster and the template, respectively. The internal structures of both the sample and template clusters are fixed (except the bond lengths of the template which are allowed to breathe by a factor $0.8 < \alpha < 1.2$ to give a better fit to that of the sample cluster) during the alignment; therefore only the rigid translation and rotation of the whole cluster are allowed during the MD simulations. After all the clusters extracted from the glass samples have been aligned respectively with the templates using the procedure described above, the motif and degree of SRO in the glass samples can be determined through the histograms of the alignment score distribution with respect to each template. The sample clusters extracted from the glass samples can be classified into different template motifs according to their smallest alignment score to the template if this score is also below the given cutoff score. Moreover, by overlapping the center atoms of the sample clusters belonging to the same template motif while keeping orientations of the clusters in their best alignment positions, the distribution of the first cluster shell atoms will also give a visible measure of the degree of the SRO motif, while the distribution of the atoms in the second and third cluster shells (and beyond) provides information about MRO motifs in the glass samples.

Crystal structure search. Unique stable and metastable crystalline structures in Al-Tb and Al-Ce alloys in the compositions close to $Al_{90}RE_{10}$ are explored using the adaptive genetic algorithm (AGA) code developed previously [35,36]. In AGA, the most time-consuming structure relaxation and energy evaluation for offspring structures in the GA loop is done efficiently by using an auxiliary interatomic potential instead of direct *ab initio* calculations. The auxiliary interatomic potential is adjusted adaptively in an adaptive loop using feedback from *ab initio* calculations on some selected structures obtained by the GA search to ensure the accuracy and reliability of the GA predictions. Different from previous AGA studies where the auxiliary interatomic potentials are analytically expressed in a given mathematical formula (e.g., LJ or EAM) with some adjustable parameters, the ANN-ML interatomic potential is used as the auxiliary interatomic potential in the present AGA search. By defining the total cost function in the ANN-ML training as a weighted sum of the errors in the energy and forces from each structure in the training database, the ANN-ML auxiliary potential during the AGA search is adaptively refined by adjusting the weight factors of different datasets. The ANN-ML potentials after such adaptive refinement describe well not only the liquid and glass structures but also crystalline structures with various bonding topologies, thus ensuring the accuracy and reliability of the discovery of the low-energy competing metastable phases in these two systems. The refined ANN-ML potentials for Al-Tb and Al-Ce systems are given in the Supplemental Material [31]. These potentials are also used in the MD simulations in this study. For a given ANN-ML potential, the GA search starts from a random generated initial structure pool. The cut-and-paste operation with some mutations implemented in the AGA code is used to generate the offspring structures from generation to generation. Structures in the Al-Tb and Al-Ce structure pools are exchanged from time to time during the GA search to enhance the diversity of the structures for each system. The GA search with a given ANN-ML potential is stopped when the lowest-energy structure in the pool is unchanged in 200 consecutive generations. Such GA protocol is repeated with newly adjusted ANN-ML potentials or newly generated initial structure pools until a sufficient number of low-energy structures with verification from *ab initio* calculations are obtained.

Ab initio calculations. The *ab initio* calculations during an AGA search and the final optimization of the metastable structures from AGA are performed based on density functional theory (DFT) using the VASP package [37,38]. The Perdew-Burke-Ernzerhof (PBE) functional [39] combined with the projector-augmented wave (PAW) method [40] and default cutoff energy in the pseudopotential is used. We use a k-point grid with a mesh size of $2\pi \times 0.02$ Å^{-1} generated by the Monkhorst-Pack scheme. This mesh size is fine enough to sample the first Brillouin zone for achieving better k-point convergence. In the final optimization of the metastable structures by DFT, the atomic positions and the lattice vectors of the unit cells are fully relaxed until the force on every atom is less than 0.01 eV/Å.

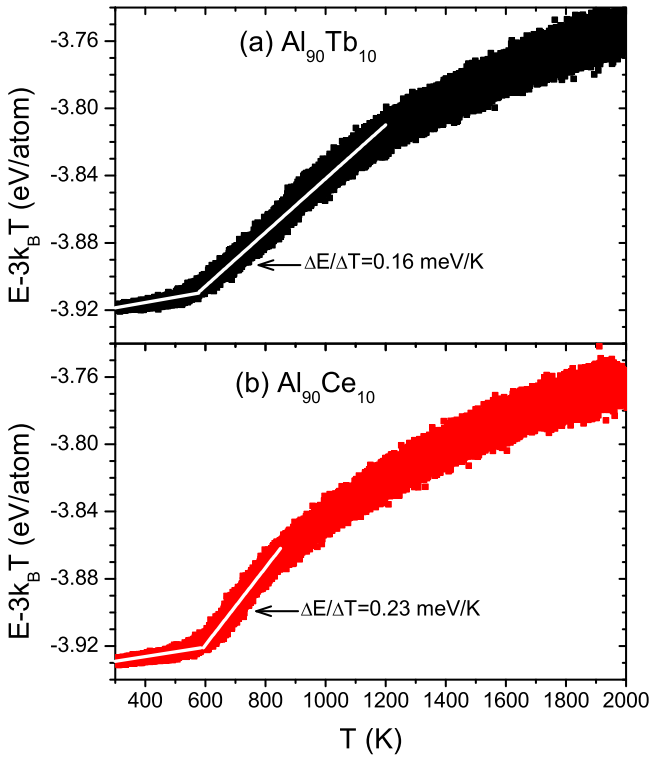

FIG. 1. The temperature dependence of potential energy E-$3k_BT$ for (a) $Al_{90}Tb_{10}$ and (b) $Al_{90}Ce_{10}$ from MD simulations.

III. RESULTS AND DISCUSSIONS

A. SRO and MRO in glasses

Figure 1 shows the temperature dependence of instantaneous potential energy E-$3k_BT$ for the $Al_{90}Tb_{10}$ and $Al_{90}Ce_{10}$ systems, respectively, during the continual cooling process with a cooling rate of 10^{10} K/s. In Fig. 1, we also plotted the white lines as a guide for the eyes to show the slope of potential energy changes. For both $Al_{90}Tb_{10}$ and $Al_{90}Ce_{10}$, the estimated glass transition temperature from the intersection point of the two white slope lines in the potential energy is about 600 K. However, the slope ($\Delta E/\Delta T$) in the region of undercooled liquid (1000–600 K) is about 0.16 meV/K for $Al_{90}Tb_{10}$ and 0.23 meV/K for $Al_{90}Ce_{10}$. It shows that the decreasing of potential energy in $Al_{90}Ce_{10}$ is faster than $Al_{90}Tb_{10}$ upon the quench process, suggesting that the atomic structure in $Al_{90}Tb_{10}$ is more sluggish than that in $Al_{90}Ce_{10}$ and the glass-forming ability (GFA) of $Al_{90}Tb_{10}$ would be greater than $Al_{90}Ce_{10}$. The suggestion of better GFA in $Al_{90}Tb_{10}$ is consistent with experimental observation [1] and will be investigated in more detail below.

The pair correlation functions and the structure factors of $Al_{90}Tb_{10}$ and $Al_{90}Ce_{10}$ at $T = 300$ K obtained from our MD simulations are compared in Fig. 2. From the total and partial pair correlation functions shown in Figs. 2(a)–2(d), we can see that the splitting of the first peak in total $g(r)$ is more obvious in $Al_{90}Ce_{10}$ than in $Al_{90}Tb_{10}$. This difference can be attributed to the fact that the bond lengths between the Al

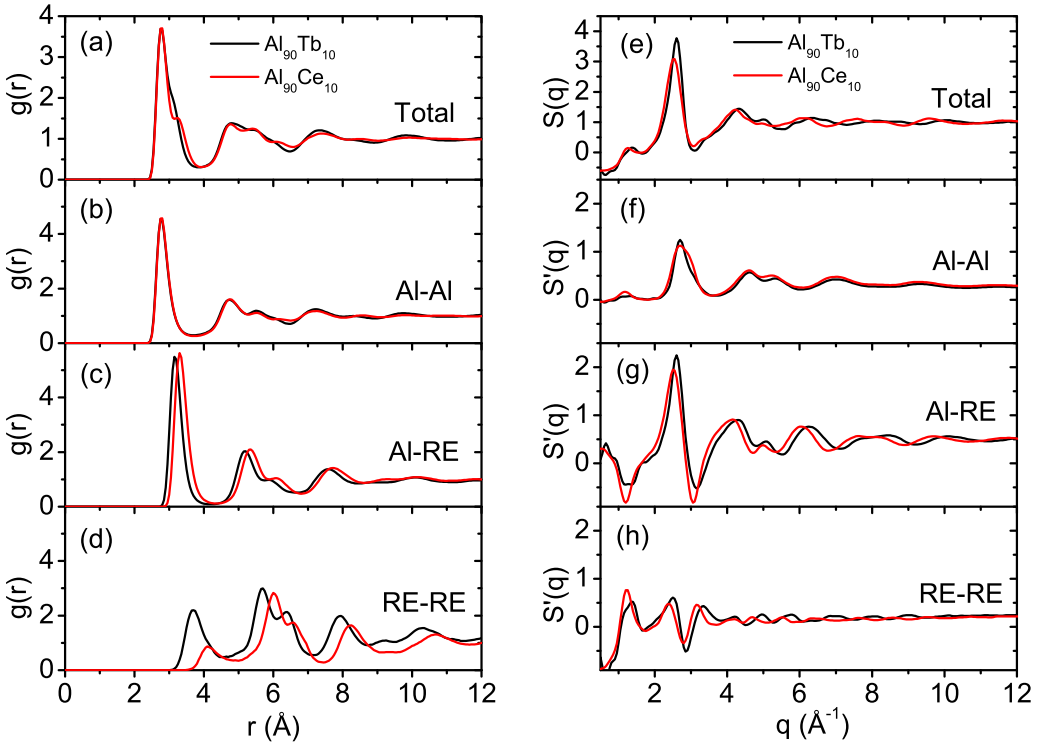

FIG. 2. (a)–(d) The total and partial pair correlation functions for $Al_{90}Tb_{10}$ and $Al_{90}Ce_{10}$ at $T = 300$ K. (e)–(h) The total and weighted partial structure factors for $Al_{90}Tb_{10}$ and $Al_{90}Ce_{10}$ at $T = 300$ K. The results of total structure factors show that the structure of $Al_{90}Tb_{10}$ is more ordered than that of $Al_{90}Ce_{10}$.

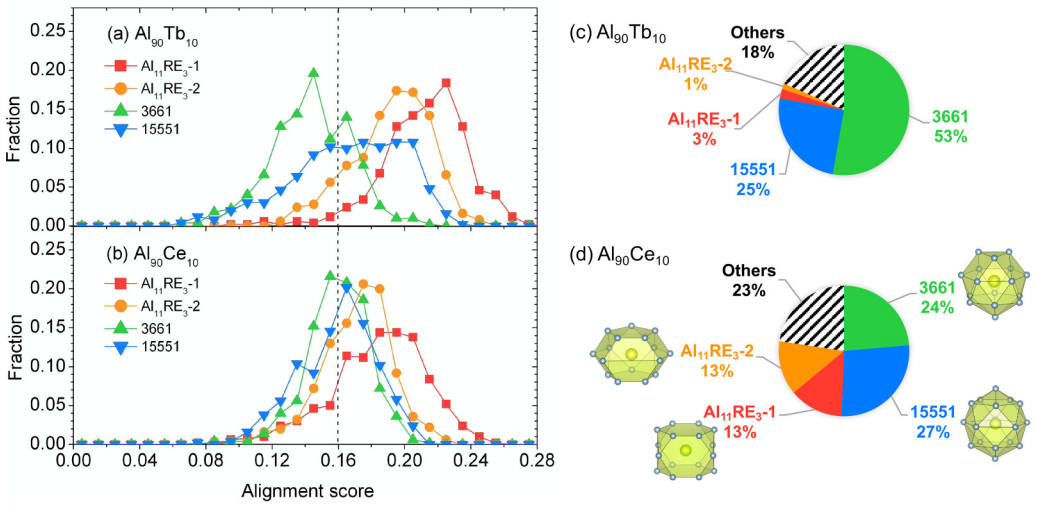

FIG. 3. The distributions of alignment scores against the relevant competing SRO templates for RE-centered clusters in the glassy (a) $Al_{90}Tb_{10}$ and (b) $Al_{90}Ce_{10}$ sample at $T = 300$ K. (c), (d) The fractions of these RE-centered SROs in $Al_{90}Tb_{10}$ and $Al_{90}Ce_{10}$, respectively. The corresponding structures of SRO templates are plotted. It shows 3661 and 15551 are the dominant SROs both in $Al_{90}Tb_{10}$ and $Al_{90}Ce_{10}$ glass samples, while only the $Al_{90}Ce_{10}$ system has considerable SRO motifs as those in $Al_{11}Ce_3$ and Hex-Al_3Ce crystal.

and RE atoms and those among the RE atoms are slightly longer in $Al_{90}Ce_{10}$ than in $Al_{90}Tb_{10}$, as one can see from the corresponding Al-RE and RE-RE partial pair correlation functions shown in Figs. 2(c) and 2(d). These results indicate that the atomic packing in $Al_{90}Tb_{10}$ glass is more compact than that in $Al_{90}Ce_{10}$ glass, consistent with the well known lanthanide contraction. The total and weighted partial structure factors (as defined in Ref. [26]) shown in Figs. 2(e)–2(h) suggest that the SRO and MRO in $Al_{90}Tb_{10}$ glass is more pronounced than those in $Al_{90}Ce_{10}$ glass, as the peaks in the structure factors of $Al_{90}Tb_{10}$ are sharper than those of $Al_{90}Ce_{10}$. These observations are also confirmed by the local structure order analysis using the cluster alignment method as discussed below.

Figures 3(a) and 3(b) show the alignment score distributions for the Tb-centered and Ce-centered clusters in the $Al_{90}Tb_{10}$ and $Al_{90}Ce_{10}$ glass samples with respect to several relevant SRO templates as labeled. The "3661" is a RE-centered cluster whose atomic shell consists of a top triangle, two consecutive hexagons in the middle and a single atom at the bottom. The "15551" is also a RE-centered cluster whose atomic shell has three consecutive pentagonal rings and is capped by an atom on the top and bottom rings, respectively. Our previous studies have shown that the 3661 and 15551 clusters are the two major RE-centered glass-forming SRO motifs in Al-rich Al-RE (RE = Sm, Tb, Ce) liquids and glasses [21,26–28,34]. $Al_{11}RE_3$-1 and $Al_{11}RE_3$-2 are the two RE-centered SRO motifs around the two nonequivalent Ce sites in $Al_{11}Ce_3$ crystal structure. For Al_3RE crystalline phase, there are two RE-centered SROs structures. One is in cubic-Al_3RE crystal (with a cubic unit cell) and the other is in hex-Al_3RE crystal (with a hexagonal unit cell), respectively. The cubic-Al_3RE crystal has fcc structures where the Al atoms occupy the face centers and the RE atoms occupy the corner of the cell. The hex-Al_3RE crystals are built by hexagonal closest-packed layers (as the $\cdots$ABABA$\cdots$ sequence) where one RE atom contacts six Al atoms. Two RE-centered clusters are extracted, respectively, from the cubic and hexagonal Al_3RE crystalline structures for the templates of the alignment analysis. By noting that the smaller alignment score indicates the sample cluster is more similar to the template, we can see from Figs. 3(a) and 3(b) that although the 3661 and 15551 clusters are dominant SROs in both glass samples, the degrees of such SROs are much stronger in the $Al_{90}Tb_{10}$ than in the $Al_{90}Ce_{10}$. On the other hand, $Al_{11}RE_3$-1 and $Al_{11}RE_3$-2 SROs are more pronounced in the $Al_{90}Ce_{10}$ than in the $Al_{90}Tb_{10}$ glass samples, although they are not as strong as the 3661 and 15551 SROs. If we use the score cutoff value of 0.16 to assign the sample clusters to the templates according to our previous studies [26–28], the fractions of the six types of SRO clusters can be quantified as shown by the pie chart in Figs. 3(c) and 3(d). We can see that in the $Al_{90}Tb_{10}$ glass sample, the 3661 and 15551 clusters are predominant with 77% of the Tb-centered clusters, while $Al_{11}RE_3$-1/2 and Al_3RE SROs are only about 5%. By contrast, in the $Al_{90}Ce_{10}$ glass sample, the percentage of the 3661 and 15551 clusters is 47% while that of $Al_{11}RE_3$-1/2 SROs is as high as 24%. Moreover, the hex-Al_3RE motif in $Al_{90}Ce_{10}$ glass is also about 10% while there is only ~2.0% of such a motif in $Al_{90}Tb_{10}$ glass, even though hex-Al_3Tb is the stable crystal with composition that is closest to ratio of 9 to 1 among all the stable Al-Tb crystalline phases. Good GFA in $Al_{90}Tb_{10}$ would be attributed to its strong tendency in forming 3661 and 15551 SRO rather than crystalline SRO motifs upon rapid solidification. On the other hand, formation of substantial crystalline SRO motifs in the $Al_{90}Ce_{10}$ would be responsible for the weaker glass-formation ability of the Al-Ce alloy. For Al-centered clusters, icosahedral and disordered icosahedral motifs are predominant SRO motifs in both glasses, as one can see from Fig. S2 in the Supplemental Material [31].

By overlapping the center atoms of the 70-atom RE-centered superclusters belonging to the same template motif while keeping orientations of the clusters in their best alignment positions, we can quantify the degrees of not only SRO

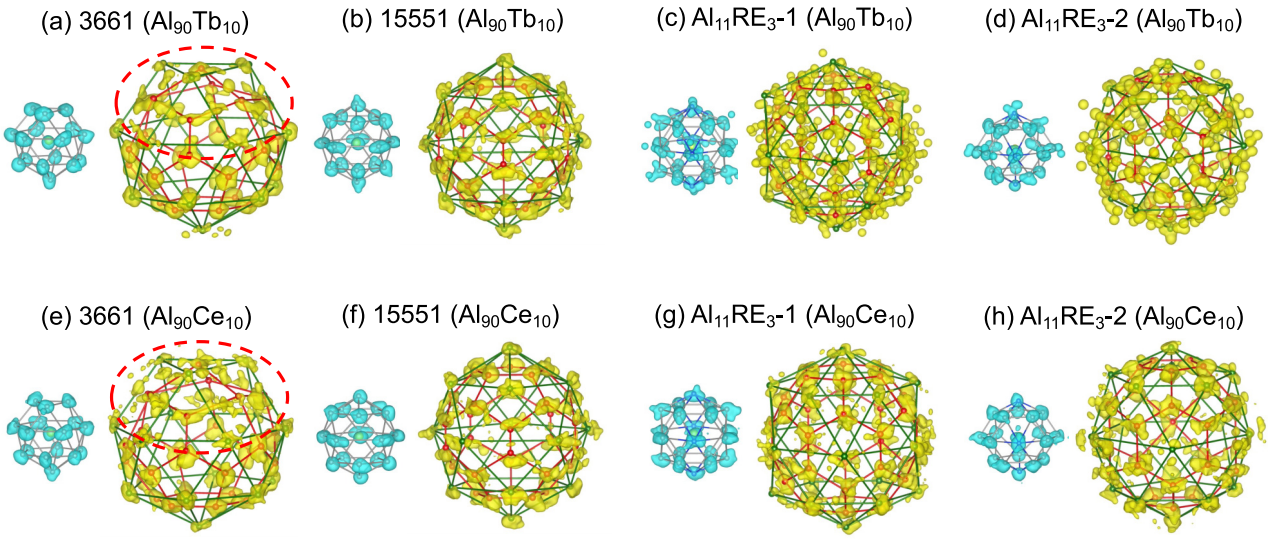

FIG. 4. The isosurface of atomic distribution density (8×10^{-6} Å^{-3}) calculated by the Gaussian smearing method for (a), (e) 3661, (b), (f) 15551, (c), (g) $Al_{11}RE_3$-1, and (d), (h) $Al_{11}RE_3$-2 superclusters (the first shell is plotted with blue and the second and third shells are in yellow) in glassy $Al_{90}Tb_{10}$ and $Al_{90}Ce_{10}$ samples, respectively. The average atomic structures are indicated by the balls and sticks in the plots. Here the stick frames outline either the SRO templates in the first shell or the average MRO structures in the second and third shells. Note that extra atoms in the first shell go beyond the $Al_{11}RE_3$-1 and $Al_{11}RE_3$-2 SRO templates in (c), (g), (d), (h).

but also the MRO of the four RE-centered motifs in the $Al_{90}Tb_{10}$ and $Al_{90}Ce_{10}$ glass samples as shown in Fig. 4. Gaussian smearing [23] is applied to the atomic distribution and the intensity of the atomic density after the Gaussian smearing has been normalized (i.e., divided) by the number of clusters used in the overlapping, so that the plots show the average structural order of the four types of dominant motifs. As shown in Figs. 4(a) and 4(b) and Figs. 4(e) and 4(f), the 3661 and 15551 SROs extend outward to form a Bergman-type MRO in the second and third shell of the superclusters. We can also see that both the first shell SRO and the MRO in the second and third cluster shells in the 3661 and 15551 motifs are very strong in both the $Al_{90}Tb_{10}$ and the $Al_{90}Ce_{10}$ glass samples. However, the MRO of the 3661 motif is stronger in the $Al_{90}Tb_{10}$ glass sample than in the $Al_{90}Ce_{10}$ glass sample, especially in the upper region of the superclusters as indicated by the red ovals in Figs. 4(a) and 4(e). On the other hand, both the SRO and MRO of the $Al_{11}RE_3$-1 and $Al_{11}RE_3$-2 motifs are much stronger in the $Al_{90}Ce_{10}$ than in the $Al_{90}Tb_{10}$ glass samples, as one can see from the comparison in Figs. 4(c) and 4(d) and Figs. 4(g) and 4(h), respectively. However, it is also interesting to note that the atoms in the second and third shells of the $Al_{11}RE_3$-1 and $Al_{11}RE_3$-2 motifs are packed in a closest-packing pattern, i.e., the outer atoms fill the hollow sites among the inner atoms, rather than being arranged as the motifs in $Al_{11}Ce_3$ crystal. Even the SRO packing of the first shell atoms in the superclusters has extra atoms capping the $Al_{11}RE_3$-1 and $Al_{11}RE_3$-2 template motifs.

B. Structure-energy landscapes

The SRO and MRO analysis suggest that while the 3661 and 15551 orders are more favored in $Al_{90}Tb_{10}$ glass, $Al_{90}Ce_{10}$ glass exhibits a stronger tendency in forming $Al_{11}Ce_3$-like structures. In order to see whether the different SRO and MRO in $Al_{90}Tb_{10}$ and $Al_{90}Ce_{10}$ glasses are driven by the different thermodynamic stabilities in the two systems, we investigate possible competing stable and metastable crystalline phases in these two systems in the vicinity of $Al_{90}RE_{10}$ composition, and correlate the structure-energy landscape of these stable and metastable crystalline structures with the dominant motifs found in the glass samples.

There are several known stable binary phases in these two systems. These known structures include $Al_{11}Ce_3$, Al_3Ce, and Al_2Ce for Al-Ce binaries and Al_3Tb, Al_2Tb, AlTb, and $AlTb_2$ for Al-Tb binaries. Using the formation energies of these known phases, the convex hulls for these two systems are shown in Fig. S3 in the Supplemental Material [31]. Our previous studies on Al-Sm [34] and Al-Tb systems [27] also identified a number of low-energy metastable Al-RE phases in the vicinity of $Al_{90}RE_{10}$ composition. These phases include $Al_{17}Tb_2$, $Al_{120}Tb_{22}$ ("big cubic phase"), α-Al_4Tb, β-Al_4Tb, and $Al_{11}Tb_3$. By placing Tb or Ce atoms at the RE positions in these structures, we optimize the structures with both *ab initio* and ANN-ML potential calculations. The formation energies for these structures obtained from our *ab initio* and ANN-ML potentials calculations are also shown in Fig. S3 [31] labeled with the cross symbols. We can see that the formation energies of these stable and metastable structures predicted from *ab initio* and ANN-ML potential calculations agree well with each other, indicating the ANN-ML potentials are accurate also in describing the energetic stability of crystalline phases in these two systems.

Based on the accurate ANN-ML potential model, we are able to perform an efficient and reliable AGA [35,36] search, as described in Sec. II, to explore additional competing metastable structures around the $Al_{90}RE_{10}$ composition in these two systems. The unit cells used in our GA search contain 39–41 atoms with the composition of $Al_{35}RE_4$, $Al_{36}RE_4$, and $Al_{37}RE_4$, respectively. The size of the structure pool

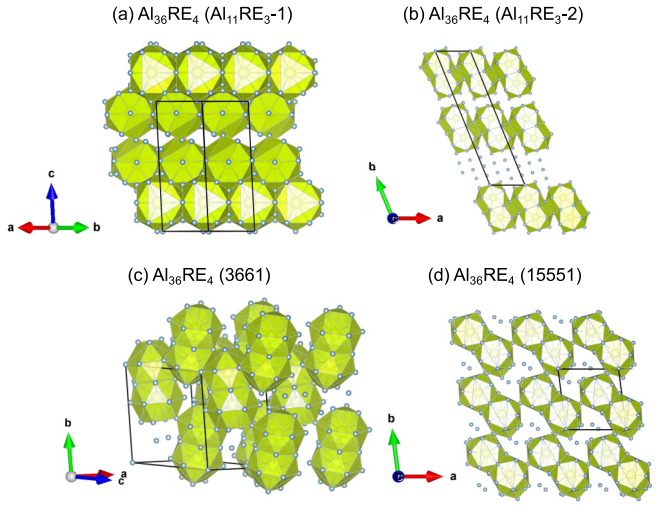

FIG. 5. Lowest-energy metastable crystal structures with different building blocks as indicated for $Al_{36}RE_4$ (RE = Tb, Ce) obtained from our AGA search. The building blocks in these crystals are (a) $Al_{11}RE_3$-1, (b) $Al_{11}RE_3$-2, (c) 3661, and (d) 15551 clusters, respectively. Note that the lowest-energy metastable crystal structures are the same for both $Al_{36}Tb_4$ and $Al_{36}Ce_4$.

during the AGA search is maintained at the level of 200 structures. The volume and shape of the unit cells are allowed to vary but the change in the length of each lattice constant does not exceed ±20% of the length of a cube of the same volume at each GA generation. The motifs of the crystal structures obtained by the AGA search are classified using the cluster alignment method described in Sec. II. The value of alignment score "cutoff 0.1" is used to assign the types of crystals obtained from GA searches.

In Fig. 5, we show the lowest-energy metastable structures built by each motif from our AGA search with the $Al_{36}RE_4$ unit cell. It is interesting to note that for each of the four motifs, the lowest-energy structures in $Al_{36}Tb_4$ and $Al_{36}Ce_4$ are the same. The corresponding lowest-energy structures for $Al_{35}RE_4$ and $Al_{37}RE_4$ unit cells are also plotted in Figs. S4 and S5 in the Supplemental Material [31]. All the lowest-energy structures in POSCAR format are given in the Supplemental Material [31]. The formation energies of these lowest-energy metastable structures with respect to the convex hull from *ab initio* and our ANN-ML potential calculations are also plotted in Fig. S3 [31]. We can see that the formation energies of these structures are very close to the corresponding convex hull (within about 80 meV/atom of the convex hull). The formation energies obtained from our ANN-ML potentials are also in very good agreement with those from *ab initio* calculations.

In order to gain more comprehensive insights into the structure-energy landscape difference in the two systems, we collect the low-energy metastable structures (within 100 meV/atom above the convex hull) belonging to the four motifs (i.e., 3661, 15551, $Al_{11}RE_3$-1, and $Al_{11}RE_3$-2), respectively, from our AGA search, and then plot their formation energy distributions as shown in Fig. 6. For Al-Tb crystals, we have 1188, 43, 527, and 27 structures in the $Al_{11}RE_3$-1, $Al_{11}RE_3$-2, 3661, and 15551 motifs respectively, while these

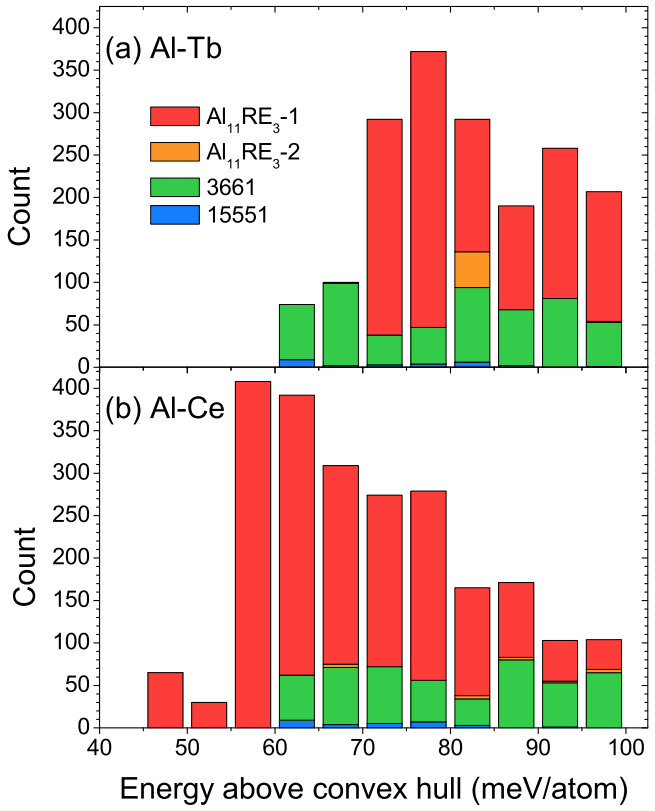

FIG. 6. The distributions of formation energies with respect to the convex hull for the low-energy metastable structures obtained from our AGA search. The structures are classified according to the four SRO motifs. The results for Al-Tb are shown in the top panel while those for Al-Ce are in the bottom panel.

numbers in the Al-Ce crystals are 1790, 17, 464, and 29, respectively. The energies in Fig. 6 are from our ANN-ML calculations. We can see that for formation energies less than 60 meV/atom above the convex hull, only the structures with $Al_{11}RE_3$-1 motifs in the Al-Ce system are found. The formation energies of the structures composed of either 3661 or 15551 motifs in both Al-Tb and Al-Ce systems are all higher than 60 meV/atom. Moreover, in the low-energy range (<70 meV/atom), the number of $Al_{11}RE_3$-1 crystals in Al-Ce is 1067 while the 3661 and 15551 crystals in the Al-Tb and Al-Ce systems are only 173 and 133, respectively. These results suggest that crystal structures with the $Al_{11}RE_3$ motif are energetically much more favorable than those with 3661 or 15551 motifs in the Al-Ce system. These results also strongly correlate with the SRO in the glass samples where a significant fraction (24%) of RE-centered clusters in $Al_{90}Ce_{10}$ glass are classified as either $Al_{11}RE_3$-1 or $Al_{11}RE_3$-2, while 3661 and 15551 motifs are predominant in the $Al_{90}Tb_{10}$ glass sample.

In addition, Table I shows the average bonding lengths of SROs in $Al_{90}Tb_{10}$ and $Al_{90}Ce_{10}$ glass as compared to that of the various competing crystalline phases at $T = 300$ K. The Tb-Al bond length of the major glass-forming SRO motifs in the glass is very different (7.0%) from that of the nearby stable Al_3Tb phase, which would make the crystallization of the Al_3Tb phase more difficult. The Ce-Al bond length of the major (3661 and 15551) SRO motifs in the glass is very

TABLE I. The average bonding lengths of the 3661 and 15551 motifs as well as the $Al_{11}RE_3$-1/2 motifs in $Al_{90}RE_{10}$ glass as compared to that of the various competing crystalline phases at $T = 300$ K. Here, the numbers in the brackets are the bonding length differences between $Al_{90}RE_{10}$ glass and the nearby stable crystalline phase. It can be seen that the Tb-Al bond length difference between the 3661+15551 motifs in $Al_{90}Tb_{10}$ and the nearby stable hex-Al_3Tb crystal is about 0.22 Å (7.0%), while the Ce-Al bond length difference between the 3661+15551 motifs in $Al_{90}Ce_{10}$ and the nearby stable $Al_{11}Ce_3$ crystal is only about 0.02 Å (0.59%).

	3661+15551 motifs in $Al_{90}RE_{10}$ (Å)	$Al_{11}RE_3$-1/2 motifs in $Al_{90}RE_{10}$ (Å)	$Al_{11}RE_3$ (Å)	Hex-Al_3RE (Å)	Cubic-Al_3RE (Å)
Al-Tb	3.324 (+0.216)	3.505 (+0.397)	3.328	3.108	3.034
Al-Ce	3.418 (+0.020)	3.558 (+0.160)	3.398	3.297	3.269

similar to that of the nearby stable $Al_{11}Ce_3$ phase, which would make the crystallization easier. Although the Ce-Al bond lengths of the $Al_{11}Ce_3$ motifs in the glass are about 4.7% larger than that in stable $Al_{11}Ce_3$ crystal, their shapes are similar which may also make the transformation easier. Therefore, thermodynamic stabilities of various competing metastable phases in the glass-formation composition region have significant influence in the glass formation and local structure orders in the glass.

C. Crystal growth kinetics

Using the ANN-ML potentials, we also performed MD simulations to study the growth of $Al_{11}RE_3$ and big-cubic-$Al_{120}RE_{22}$ phases at the interface with $Al_{90}RE_{10}$ liquids where the RE is Tb and Ce, respectively. While $Al_{11}RE_3$-1 and $Al_{11}RE_3$-2 SRO motifs are the building blocks of the $Al_{11}RE_3$ crystalline phase, the RE-centered SRO motifs in the big-cubic-$Al_{120}RE_{22}$ phase are 3661 and 16661, respectively. The 16661 motif is not the same as, but has structure topology very similar to, the 15551 clusters observed in the $Al_{90}Tb_{10}$ and $Al_{90}Ce_{10}$ glasses. Therefore, comparing the growth behavior and speed of these two crystalline phases from the solid/liquid interfaces would provide useful insights into the phase selection kinetics in the Al-Tb system vs the Al-Ce system.

The temperature in the simulations of crystal growth is 700 K for both the Al-Tb and Al-Ce systems. We chose 700 K for the crystal growth simulation because it is just slightly above the T_g in the two systems. From Fig. 1 the glass transition temperatures of $Al_{90}Tb_{10}$ and $Al_{90}Ce_{10}$ estimated from the intersection point of the two white slope lines in the potential energy are very close to each other around 600 K. According to the phase diagram in the Supplemental Material [31], the melting temperatures of Al-Tb and Al-Ce at 90-10 composition are also very close to each other. Therefore, the degree of undercooling at 700 K ($T/T_m \approx 0.5$) should be similar in the two systems. As discussed above, although the melting and glass transition temperatures are similar in these two systems, the change in the potential energy with temperature in the undercooled liquid region is more rapid in $Al_{90}Ce_{10}$ than in $Al_{90}Tb_{10}$, suggesting $Al_{90}Ce_{10}$ should have better crystallization ability. Therefore, the main purpose of crystal growth simulations is to estimate the crystal growth speed at the temperature just above the T_g in order to compare the GFA in the two systems.

To prepare an initial solid/liquid interface, we first perform MD simulation for the crystalline structure at $T = 700$ K for 10 ps. The MD simulation box has a rectangular shape and contains 2016 atoms for the $Al_{11}RE_3$ phase and 2272 atoms for the big-cubic-$Al_{120}RE_{22}$ phase, respectively. Periodic boundary conditions are applied in the three directions. Then, the atoms in the left half of the MD simulation box are kept fixed at their instant positions at 700 K, while the atoms in the right half of the MD simulation box are heated to 2000 K for 1 ns to ensure the structure in this half of the box is completely melted into a liquid state. During the MD simulation at 2000 K, some of the Al atoms are randomly selected to switch to RE atoms in order to have liquid composition at $Al_{90}RE_{10}$. Finally, the liquid is cooled down to $T = 700$ K with a cooling rate of 10^{13} K/s. Thus, an initial solid/liquid interface is prepared at $T = 700$ K where the solid part is in the given crystalline structure ($Al_{11}RE_3$ or $Al_{120}RE_{22}$) while the liquid part has a composition of $Al_{90}RE_{10}$. We denote this initial interface structure as the $t = 0$ configuration. Starting from the $t = 0$ configuration, MD simulations are performed at a constant temperature of 700 K and constant $P = 0$ to study the growth of the crystal.

In Fig. 7, we compare the growth speed of the $Al_{11}RE_3$ and $Al_{120}RE_{22}$ phases for RE = Tb or Ce, respectively. Only the growth along the (001) direction is shown in Fig. 7. Growth behavior along other directions is similar to that along the (001) directions, as shown by Fig. S6 in the Supplemental Material [31]. The short movies of crystal growth (t = 0–200 ns) are also given in the Supplemental Material [31]. From the plots in Fig 7, we can see that the growth speed of the $Al_{11}RE_3$ phase in the Al-Ce system is slightly faster than the growth in the Al-Tb system. At 60 ns, crystallization in the Al-Ce system is essentially completed; it takes about 130 ns for the Al-Tb system to reach the same degree of crystallization. Because RE concentration is about 21.4% in the $Al_{11}RE_3$ phase, the crystallization of the $Al_{11}RE_3$ phase in the MD simulation will saturate when all the RE atoms in the $Al_{90}RE_{10}$ liquid have been incorporated into the crystalline phase, thus leaving a pure Al slab in the MD simulation box as seen from Fig. 7. For the big-cubic-$Al_{120}RE_{22}$ phase, the crystal growth is much faster in Al-Ce than in the Al-Tb system. Crystallization in the whole MD simulations cell has already been reached before 60 ns in the Al-Ce system, while the crystal growth in the Al-Tb system is still not quite completed even at the simulation time of 130 ns as one can see from the plots in Fig. 7.

In order to confirm the results of a faster crystal growth rate for Al-Ce, we also simulated the crystal growth at T = 800 K for Al-Ce, where the degree of undercooling is smaller

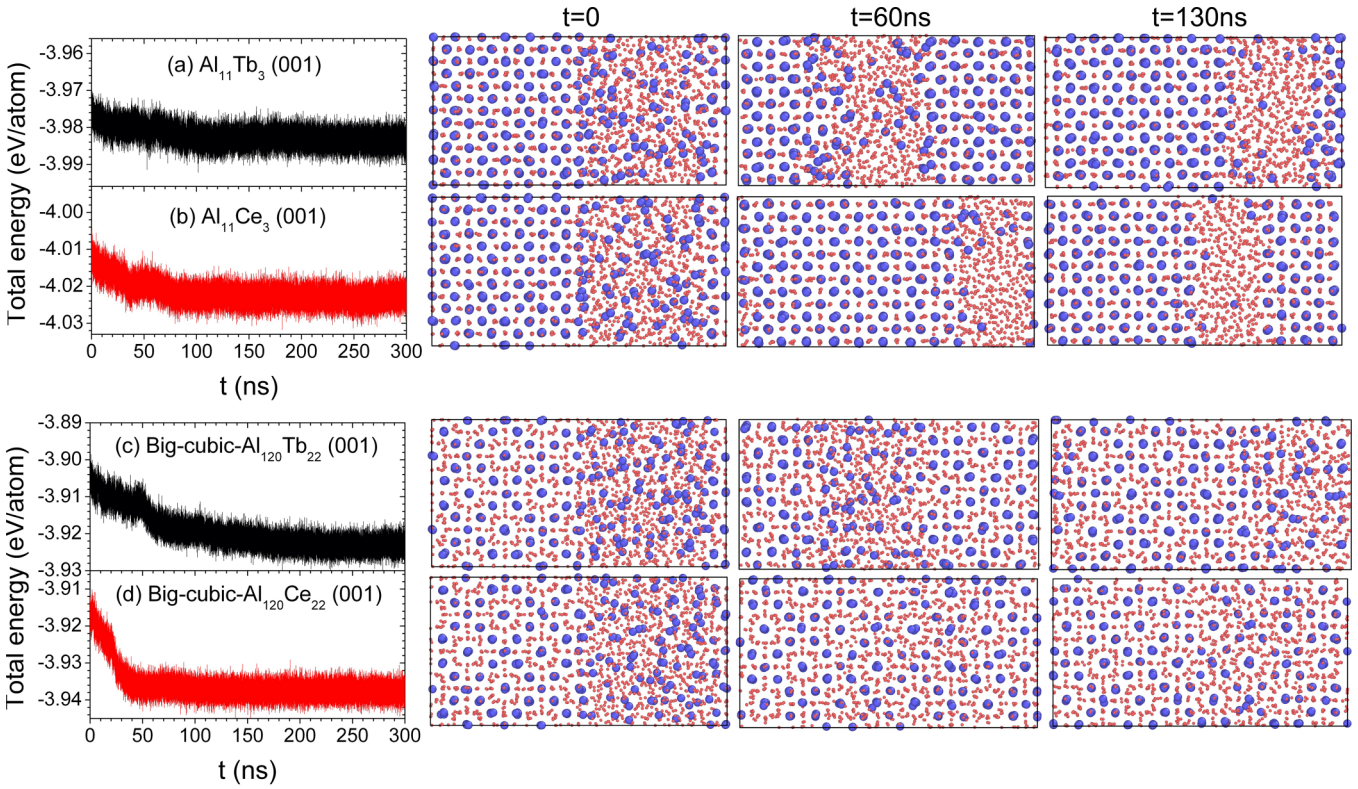

FIG. 7. The change in total energy during the annealing process of (a), (b) $Al_{11}RE_3$ and (c), (d) big-cubic-$Al_{120}RE_{22}$ at $T = 700$ K. The solid/liquid interfaces are along the directions of (001), where the liquid is $Al_{90}RE_{10}$. The snapshots at initial $t = 0$, and annealing times $t = 60$ ns and $t = 130$ ns are also shown on the right. The blue and red dots represent the RE and Al atoms, respectively.

than that of 700 K. As shown in Fig. S7 of the Supplemental Material [31], the crystal growth on Al-Ce at 800 K is still faster than the Al-Tb system at 700 K.

We found that the difference in the crystal growth speed of the two systems is correlated with the diffusivity of the RE atoms in the undercooled liquid. The mean square displacements (MSDs) as the function of time for Al atoms and RE atoms in the undercooled liquid at 700 K are shown in Fig. 8.

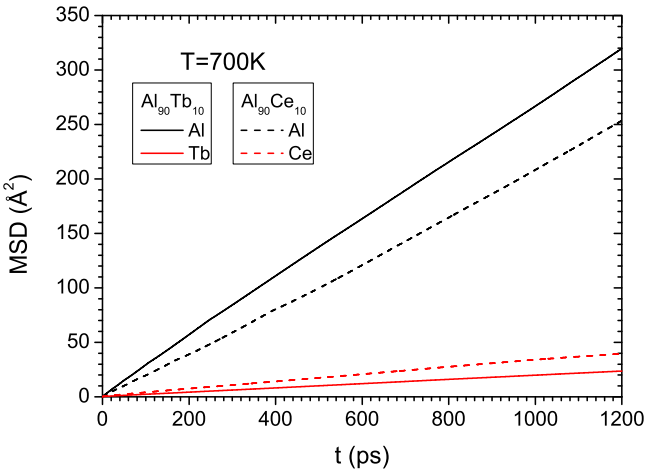

FIG. 8. The mean square displacements (MSDs) as a function of time for Al atoms and RE atoms in the undercooled $Al_{90}Tb_{10}$ and $Al_{90}Ce_{10}$ liquids at 700 K.

Using the Einstein formula, the diffusion constants of Al and Tb atoms in the $Al_{90}Tb_{10}$ undercooled liquid are 0.44×10^{-5} and 0.032×10^{-5} cm^2/s, respectively, while the diffusion constants of Al and Ce atoms in the $Al_{90}Ce_{10}$ undercooled liquid are 0.35×10^{-5} and 0.055×10^{-5} cm^2/s. We can see that although Al atoms move faster in $Al_{90}Tb_{10}$ undercooled liquid at 700 K, Tb atoms move considerably slower than Ce atoms. The limiting factor for the growth of the crystalline phases is the mobility of the RE atoms. These results indicate that the crystallization kinetics for Al-Tb is slower than that for Al-Ce crystals, which again implies that the Al-Ce system has a stronger tendency for crystal forming than the Al-Tb system.

Based on Wilson-Frenkel theory [41,42], the crystal growth rate is proportional to the diffusion coefficient. Although the diffusion constant of Ce is slightly larger than that of Tb, as shown in Fig. 8, the difference would not be sufficient to explain the crystal growth difference in these two systems. In order to further understand the difference of crystal growth between the Al-Tb and the Al-Ce systems, we calculated the enthalpy difference between liquid and crystal (the latent heat) for $Al_{11}RE_3$ and big-cubic-$Al_{120}RE_{22}$. Supercell samples of $9 \times 4 \times 3$ $Al_{11}RE_3$ (total 3024 atoms) and a $3 \times 3 \times 3$ big-cubic-$Al_{120}RE_{22}$ (total 3834 atoms) are generated for MD simulation, respectively. The samples are first equilibrated with an *NPT* ensemble at $T = 300$ K for 500 ps and then heated to 2000 K at a rate of 10^{12} K/s. During the heating process where the samples are not melted, snapshots at $T = 700$ to 1100 K with 100 K intervals are

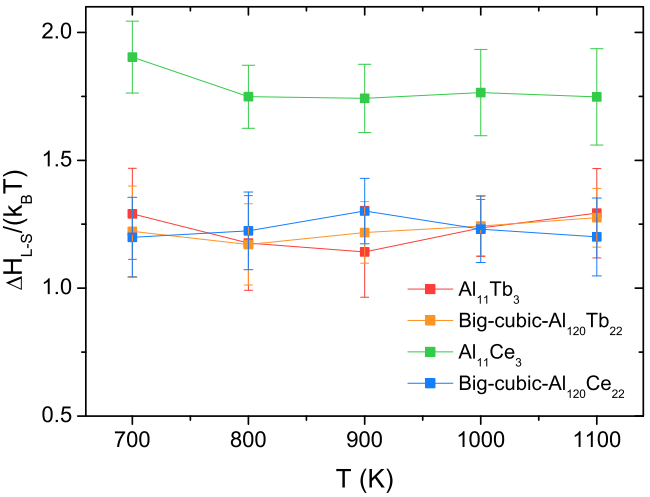

FIG. 9. The latent heats of $Al_{11}RE_3$ and big-cubic-$Al_{120}RE_{22}$ scaled by the thermal energy.

taken as initial structures to perform MD simulations at the given temperature for 25 ps to obtain the average enthalpy of crystal at this temperature. At high temperature $T = 2000$ K, the samples are melted into liquid and then equilibrated for 500 ps. The liquid samples are then cooled at a rate of 10^{12} K/s to $T = 700$ K. The snapshots of undercooled liquid samples from $T = 700$ to 1100 K with 100 K intervals are also selected as the initial configuration for 25 ps MD simulation to obtain the average enthalpy of the liquid at the given temperature.

The enthalpy difference between the liquid and crystal scaled by thermal energy for $Al_{11}RE_3$ and big-cubic-$Al_{120}RE_{22}$ at different temperatures is shown in Fig. 9. It shows that for Al-Tb crystals, the driving forces of $Al_{11}Tb_3$ and big-cubic-$Al_{120}Tb_{22}$ are close to each other. Therefore, these two crystalline phases both have no competitive advantages in crystal growth at a solid/liquid interface, which leads to frustration and inefficient crystallization. However, the crystallization driving force of $Al_{11}Ce_3$ is about 1.5 times as large as that of the other crystalline phases. Thus, the crystallization of $Al_{11}Ce_3$ should be more efficient (see our crystal growth simulations in Fig. 7). Although the driving force of big-cubic-$Al_{120}Ce_{22}$ is smaller and close to that of the Al-Tb system, the crystallization is still more efficient than that in the Al-Tb system since the chemical order of the SRO clusters in $Al_{90}Ce_{10}$ liquid is closer to that in crystal structures. On the contrary, the chemical frustration in the Al-Tb system could hinder crystallization and lead to better GFA in the Al-Tb system.

The crystal growth difference between Al-Tb and Al-Ce can also be attributed to the different chemical orders in RE-centered SRO clusters in the undercooled liquids. To examine the chemical order in the SRO clusters, we plotted the distributions of the atoms in the first shell of the RE-centered SRO clusters after the alignment, as shown in Fig. 10(a). The structures and chemical orders of some competing crystalline Al-RE phases are also plotted in Figs. 10(b)–10(d) for reference. As shown in Fig. 10(a), the RE atoms are nearly uniformly distributed around all the vertices of the first shell in SRO clusters, except that in 3661 SROs the RE atoms prefer occupying the bottom vertex indicated as "1" in 3661. This feature is also observed in the big-cubic-$Al_{122}RE_{22}$ crystal where the 3661 SRO is the building block of the structure. The average compositions of RE atoms in the first shell of SROs are also calculated for $Al_{90}Tb_{10}$ and $Al_{90}Ce_{10}$, where atoms at vertex 1 of 3661 SRO are excluded from statistical analysis. The results show the RE composition in $Al_{90}Tb_{10}$ SRO clusters is larger than that for $Al_{90}Ce_{10}$. For the glass-forming 3661 and 15551 SROs (which are the majority in $Al_{90}RE_{10}$), RE composition is ~8% and ~5%, respectively, in $Al_{90}Tb_{10}$ glass, as compared to ~3% in $Al_{90}Ce_{10}$ glass. Even for crystal-SRO clusters in the glass phase, the RE composition at the first shell is larger in $Al_{90}Tb_{10}$ than in $Al_{90}Ce_{10}$.

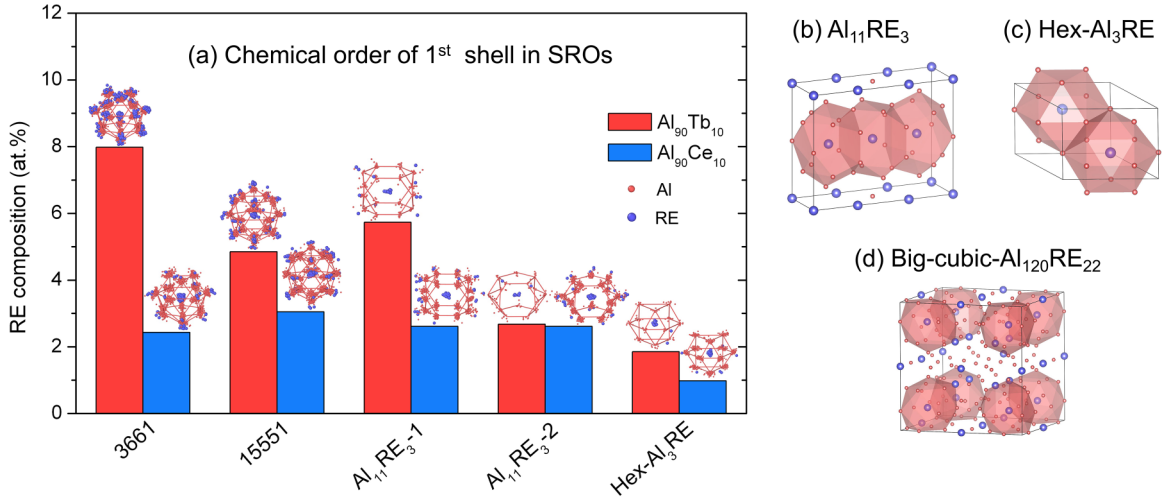

FIG. 10. (a) The RE composition of the first shell in RE-centered SROs for $Al_{90}Tb_{10}$ and $Al_{90}Ce_{10}$. The corresponding atom distributions of SROs after aligning against templates are also plotted in (a). The structures of some competing crystalline phases in $Al_{90}RE_{10}$ liquid are plotted in (b)–(d), where the red polyhedra with Al atoms vertices are the RE-centered SRO clusters as building blocks in crystals. (b) $Al_{11}RE_3$, (c) hex-Al_3RE, and (d) big-cubic-$Al_{120}RE_{22}$, where the red polyhedra are 3661 clusters.

Note that all the atoms are Al in the first shell of RE-centered motifs in competing crystalline phases (note that vertex 1 is excluded from the statistics), as shown in Figs. 10(b)–10(d).

Therefore, in comparison with $Al_{90}Tb_{10}$ glass, the SRO clusters in $Al_{90}Ce_{10}$ glass are not only structurally more similar to the crystal phases but also with chemical order closer to that of the crystal phases. Less deviation of structural and chemical orders from competing crystalline phases for the SROs in $Al_{90}Ce_{10}$ undercooled liquid can reduce both the geometrical and chemical frustration against crystallization [43–47]. Because chemical order difference in the liquid and crystalline phases determines the interface energy which dominates the crystallization [43], the primary barrier to crystallization is lowered for glass SROs in $Al_{90}Ce_{10}$. Thus, besides the fact that there is a noticeable fraction of crystal SROs in $Al_{90}Ce_{10}$, the lesser deviation of chemical order from competing crystals for all the SROs in $Al_{90}Ce_{10}$ would also enhance the crystallization and weaken the GFA in $Al_{90}Ce_{10}$ compared to the case of $Al_{90}Tb_{10}$.

IV. SUMMARY

Using the accurate and transferable interatomic potentials based on ANN-ML, we have performed reliable MD simulations and cluster alignment analysis to compare the similarity and difference of SRO and MRO in $Al_{90}Tb_{10}$ and $Al_{90}Ce_{10}$ metallic glasses. Our results show that although the glass-forming Ce-centered 3661 and 15551 clusters are also the major motifs in $Al_{90}Ce_{10}$ glass, the percentage of such motifs (47%) is substantially smaller than that in $Al_{90}Tb_{10}$ glass which encompasses 77% of the Tb-centered clusters. On the other hand, there is a significant amount of $Al_{11}Ce_3$ (24% of Ce-centered clusters) and Al_3Ce (10% of Ce-centered cluster) crystalline SRO clusters in $Al_{90}Ce_{10}$ glass, while the crystalline motifs are negligible in $Al_{90}Tb_{10}$ glass. The SRO and MRO differences in the two glasses can be attributed to the preference of different crystalline phases in the Al-Ce system vs the Al-Tb system. We explored possible competing stable and metastable crystalline phases in these two systems in the vicinity of $Al_{90}RE_{10}$ composition using the AGA method and the ANN-ML interatomic potentials. A significant number of metastable crystalline structures with formation energy within 100 meV/atom above the corresponding convex hulls have been discovered from our AGA search. These low-energy structures can be classified into the four major structure motifs, i.e., 3661, 15551, $Al_{11}RE_3$-1, and $Al_{11}RE_3$-2, which are observed in the glass samples. We found that the structures with $Al_{11}RE_3$-1 and $Al_{11}RE_3$-2 motifs are energetically more favorable in the Al-Ce system, while those with 3661 and 15551 are preferred in the Al-Tb system. These structure-energy landscapes are strongly correlated with the SRO and MRO found in the two glasses, suggesting thermodynamic driving forces play an important role in the phase selections. We also found that due to the difference in the atomic size and interatomic interaction between Al-Ce and Al-Tb systems, the average Tb-Al bond lengths in the glasses are more than 7.0% larger than that in the nearby stable crystalline Al_3Tb phase. Such large RE-Al bond length difference would also make crystallization in the Al-Tb system harder. Crystallization simulations using MD based on a solid/liquid interface model also show that the speed of crystal growth in the Al-Ce system is about 2-3 times faster than that in the Al-Tb system at a similar undercooling condition. By comparing atomic diffusion constants in the undercooled liquids and the crystal-liquid latent heats of several competing crystalline structures, we found that the crystallization driving forces are mainly from the enthalpy difference between liquid and crystal structures. Moreover, we showed that less deviation of chemical order from competing crystals for all the SROs in $Al_{90}Ce_{10}$ would also enhance the crystallization and weaken the GFA in $Al_{90}Ce_{10}$ as compared to the case of $Al_{90}Tb_{10}$. The results from our studies are consistent with experimental observation that Al-Tb exhibits much better GFA than Al-Ce, and crystalline phase formations are more robust in the Al-Ce system. Our studies provide in-depth insights into the phase selection and formation difference between Al-LRE and Al-HRE metallic alloys.

The data that support the findings of this study are available from the corresponding author upon reasonable request.

ACKNOWLEDGMENTS

Work at Ames Laboratory was supported by the U.S. Department of Energy (DOE), Office of Science, Basic Energy Sciences, Materials Science and Engineering Division including a grant of computer time at the National Energy Research Supercomputing Center (NERSC) in Berkeley. Ames Laboratory is operated for the U.S. DOE by Iowa State University under Contract No. DE-AC02-07CH11358. L.T. acknowledges the support by the National Natural Science Foundation of China (Grant No. 11304279).

The authors declare no competing interests.

[1] A. Inoue, Amorphous, nanoquasicrystalline and nanocrystalline alloys in Al-based systems, Prog. Mater Sci. **43**, 365 (1998).

[2] D. V. Louzguine and A. Inoue, Crystallization behaviour of Al-based metallic glasses below and above the glass-transition temperature, J. Non-Cryst. Solids **311**, 281 (2002).

[3] D. V. Louzguine-Luzgin and A. Inoue, Comparative study of the effect of cold rolling on the structure of Al–RE–Ni–Co (RE = rare−earth metals) amorphous and glassy alloys, J. Non-Cryst. Solids **352**, 3903 (2006).

[4] T. Egami, The atomic structure of aluminum based metallic glasses and universal criterion for glass formation, J. Non-Cryst. Solids **205–207**, 575 (1996).

[5] J. H. Perepezko, R. J. Hebert, and W. S. Tong, Amorphization and nanostructure synthesis in Al alloys, Intermetallics **10**, 1079 (2002).

[6] K. Saksl, P. Jóvári, H. Franz, Q. S. Zeng, J. F. Liu, and J. Z. Jiang, Atomic structure of $Al_{89}La_6Ni_5$ metallic glass, J. Phys.: Condens. Matter **18**, 7579 (2006).

[7] R. J. Hebert, J. H. Perepezko, H. Rösner, and G. Wilde, Dislocation formation during deformation-induced synthesis of

nanocrystals in amorphous and partially crystalline amorphous $Al_{88}Y_7Fe_5$ alloy, Scr. Mater. **54**, 25 (2006).

[8] A. K. Gangopadhyay, T. K. Croat, and K. F. Kelton, The effect of phase separation on subsequent crystallization in $Al_{88}Gd_6La_2Ni_4$, Acta Mater. **48**, 4035 (2000).

[9] K. K. Sahu, N. A. Mauro, L. Longstreth-Spoor, D. Saha, Z. Nussinov, M. K. Miller, and K. F. Kelton, Phase separation mediated devitrification of $Al_{88}Y_7Fe_5$ glasses, Acta Mater. **58**, 4199 (2010).

[10] Q. Luo and W. H. Wang, Rare earth based bulk metallic glasses, J. Non-Cryst. Solids **355**, 759 (2009).

[11] X. M. Li, Y. Wang, J. J. Yi, L. T. Kong, and J. F. Li, Influence of substitution of La by Gd on crystallization behavior of Al-Ni-La metallic glasses, J. Alloys Compd. **790**, 626 (2019).

[12] W. G. Stratton, J. Hamann, J. H. Perepezko, P. M. Voyles, X. Mao, and S. V. Khare, Aluminum nanoscale order in amorphous $Al_{92}Sm_8$ measured by fluctuation electron microscopy, Appl. Phys. Lett. **86**, 141910 (2005).

[13] Z. C. Sims, D. Weiss, S. K. McCall, M. A. McCuire, R. T. Ott, T. Ceer, O. R. Rios, and P. E. A. Turchi, Cerium-based, intermetallic-strengthened aluminum casting alloy: High-volume co-product development, JOM **68**, 1940 (2016).

[14] Z. C. Sims, O. R. Rios, D. Weiss, P. E. A. Turchi, A. Perron, J. R. I. Lee, T. T. Li, J. A. Hammons, M. Bagge-Hansen, T. M. Willey, K. An, Y. Chen, A. H. King, and S. K. McCall, High performance aluminum–cerium alloys for high-temperature applications, Mater. Horiz. **4**, 1070 (2017).

[15] A. Plotkowski, O. Rios, N. Sridharan, Z. Sims, K. Unocic, R. Ott, R. Dehoff, and S. S. Babu, Evaluation of an Al-Ce alloy for laser additive manufacturing, Acta Mater. **126**, 507 (2017).

[16] R. Castilloux, Rare Earth Elements: Market Issues and Outlook, http://www.adamasintel.com/wp-content/uploads/2019/07/Adamas-Intelligence-Rare-Earths-Market-Issues-and-Outlook-Q2-2019.pdf, Adamas Intelligence (2019).

[17] S. B. Castor, Rare earth deposits of North America, Resour. Geol. **58**, 337 (2008).

[18] Y. E. Kalay, I. Kalay, J. Hwang, P. M. Voyles, and M. J. Kramer, Local chemical and topological order in Al–Tb and its role in controlling nanocrystal formation, Acta Mater. **60**, 994 (2012).

[19] L. Jin, Y.-B. Kang, P. Chartrand, and C. D. Fuerst, Thermodynamic evaluation and optimization of Al–Gd, Al–Tb, Al–Dy, Al–Ho and Al–Er systems using a modified quasichemical model for the liquid, CALPHAD **34**, 456 (2010).

[20] X. W. Fang, C. Z. Wang, Y. X. Yao, Z. J. Ding, and K. M. Ho, Atomistic cluster alignment method for local order mining in liquids and glasses, Phys. Rev. B **82**, 184204 (2010).

[21] Y. Sun, Y. Zhang, F. Zhang, Z. Ye, Z. Ding, C.-Z. Wang, and K.-M. Ho, Cooling rate dependence of structural order in $Al_{90}Sm_{10}$ metallic glass, J. Appl. Phys. **120**, 015901 (2016).

[22] Y. Zhang, F. Zhang, C.-Z. Wang, M. I. Mendelev, M. J. Kramer, and K.-M. Ho, Cooling rates dependence of medium-range order development in $Cu_{64.5}Zr_{35.5}$ metallic glass, Phys. Rev. B **91**, 064105 (2015).

[23] X. W. Fang, C. Z. Wang, S. G. Hao, M. J. Kramer, Y. X. Yao, M. I. Mendelev, Z. J. Ding, R. E. Napolitano, and K. M. Ho, Spatially resolved distribution function and the medium-range order in metallic liquid and glass, Sci. Rep. **1**, 194 (2011).

[24] Z. Ye, F. Zhang, Y. Sun, M. C. Nguyen, M. I. Mendelev, R. T. Ott, E. Park, M. F. Besser, M. J. Kramer, Z. Ding, C. Z. Wang, and K. M. Ho, Structural hierarchy as a key to complex phase selection in Al-Sm, Phys. Rev. Mater. **1**, 055601 (2017).

[25] H. Wang, L. Zhang, J. Han, and E W., DEEPMD-KIT: A deep learning package for many-body potential energy representation and molecular dynamics, Comput. Phys. Commun. **228**, 178 (2018).

[26] L. Tang, Z. J. Yang, T. Q. Wen, K. M. Ho, M. J. Kramer, and C. Z. Wang, Development of interatomic potential for Al–Tb alloys using a deep neural network learning method, Phys. Chem. Chem. Phys. **22**, 18467 (2020).

[27] L. Tang, Z. J. Yang, T. Q. Wen, K. M. Ho, M. J. Kramer, and C. Z. Wang, Short- and medium-range orders in $Al_{90}Tb_{10}$ glass and their relation to the structures of competing crystalline phases, Acta Mater. **204**, 116513 (2021).

[28] L. Tang, K. M. Ho, and C. Z. Wang, Molecular dynamics simulation of metallic Al-Ce liquids using a neural network machine learning interatomic potential, J. Chem. Phys. **155**, 194503 (2021).

[29] A. Jain, S. P. Ong, G. Hautier, W. Chen, W. D. Richards, S. Dacek, S. Cholia, D. Gunter, D. Skinner, G. Ceder, and K. A. Persson, The Materials Project: A materials genome approach to accelerating materials innovation, APL Mater. **1**, 011002 (2013).

[30] S. Plimpton, Fast parallel algorithms for short-range molecular dynamics, J. Comput. Phys. **117**, 1 (1995).

[31] See Supplemental Material at http://link.aps.org/supplemental/10.1103/PhysRevMaterials.7.025601 for comparison of ANN-ML potential predicted properties with experimental and DFT data, SROs of Al-centered clusters, lowest-energy metastable crystal structures, crystal growth from solid/liquid interface, and phase diagrams.

[32] S. Nosé, A unified formulation of the constant temperature molecular dynamics methods, J. Chem. Phys. **81**, 511 (1984).

[33] W. G. Hoover, Canonical dynamics: Equilibrium phase-space distributions, Phys. Rev. A **31**, 1695 (1985).

[34] D. M. Deaven and K. M. Ho, Molecular Geometry Optimization with a Genetic Algorithm, Phys. Rev. Lett. **75**, 288 (1995).

[35] S. Q. Wu, M. Ji, C. Z. Wang, M. C. Nguyen, X. Zhao, K. Umemoto, R. M. Wentzcovitch, and K. M. Ho, An adaptive genetic algorithm for crystal structure prediction, J. Phys.: Condens. Matter **26**, 035402 (2014).

[36] G. Kresse and J. Furthmuller, Efficient iterative schemes for *ab initio* total-energy calculations using a plane-wave basis set, Phys. Rev. B **54**, 11169 (1996).

[37] G. Kresse and J. Furthmuller, Efficiency of *ab-initio* total energy calculations for metals and semiconductors using a plane-wave basis set, Comput. Mater. Sci. **6**, 15 (1996).

[38] J. P. Perdew, K. Burke, and M. Ernzerhof, Generalized Gradient Approximation Made Simple, Phys. Rev. Lett. **77**, 3865 (1996).

[39] D Vanderbilt, Soft self-consistent pseudopotentials in a generalized eigenvalue formalism, Phys. Rev. B **41**, 7892 (1990).

[40] Y. Sun, F. Zhang, Z. Ye, Y. Zhang, X. Fang, Z. Ding, C.-Z. Wang, M. I. Mendelev, R. T. Ott, M. J. Kramer, and K.-M. Ho, 'Crystal genes' in metallic liquids and glasses, Sci. Rep. **6**, 23734 (2016).

[41] H. W. Wilson, On the velocity of solidification and viscosity of super-cooled liquids, London, Edinburgh Dublin Philos. Mag. J. Sci. **50**, 238 (1900).

[42] J. Frenkel, *Kinetic Theory of Liquids* (The Clarendon Press, Oxford, 1946).

[43] Y.-C. Hu and H. Tanaka, Physical origin of glass formation from multicomponent systems, Sci. Adv. **6**, eabd2928 (2020).

[44] Y. C. Hu and H. Tanaka, Revealing the role of liquid preordering in crystallization of supercooled liquids, Nat. Commun. **13**, 4519 (2022).

[45] Y.-C. Hu, W. Jin, J. Schroers, M. D. Shattuck, and C. S. O'Hern, Glass-forming ability of binary Lennard-Jones systems, Phys. Rev. Mater. **6**, 075601 (2022).

[46] Y.-C. Hu, J. Schroers, M. D. Shattuck, and C. S. O'Hern, Tuning the glass-forming ability of metallic glasses through energetic frustration, Phys. Rev. Mater. **3**, 085602 (2019).

[47] Y.-C. Hu, K. Zhang, S. A. Kube, J. Schroers, M. D. Shattuck, and C. S. O'Hern, Glass formation in binary alloys with different atomic symmetries, Phys. Rev. Mater. **4**, 105602 (2020).